East European Journal of Physics. **2.** 297-312 (2025)
DOI:10.26565/2312-4334-2025-2-37 ISSN 2312-4334

EFFECT OF DEPOSITION CONDITIONS ON MICROSTRUCTURE AND COMPOSITION OF NITRIDE MONOLAYER AND CARBIDE-NITRIDE MULTILAYER COATINGS BASED ON W AND Nb

O.V. Maksakova[a,b], V.M. Beresnev[b], S.V. Lytovchenko[b], D.V. Horokh[b], B.O. Mazilin[b], I.O. Afanasieva[b], M. Čaplovičova[c], M. Sahul[a]

[a]*Institute of Materials Science, Slovak University of Technology in Bratislava, 25, Jána Bottu Str., 917 24 Trnava, Slovakia*
[b]*V.N. Karazin Kharkiv National University, 4, Svoboby Sq., 61000 Kharkiv, Ukraine*
[c]*Centre for Nanodiagnostics of Materials, Slovak University of Technology in Bratislava, Vazovova 5, 812 43 Bratislava, Slovakia*
**Corresponding Author e-mail*: *s.lytovchenko@karazin.ua*
Received March 5, 2025; revised April 27, accepted May 19, 2025

This study investigates the structural and compositional evolution of monolayer WNbN and multilayer WNbN/WNbC coatings deposited by the cathodic arc evaporation. The effects of substrate bias voltage (–50 V to –200 V) and cathode arc current (130 – 150 A for W, 110 – 120 A for Nb) were systematically studied to tailor coating morphology, phase formation, and elemental distribution. Cross-sectional microstructural analysis revealed pseudo-multilayer structures within monolayers due to substrate rotation and limited interdiffusion. Increasing bias voltage promoted densification, grain refinement, and improved adhesion, but also enhanced the re-sputtering of nitrogen, affecting stoichiometry and deposition rates. Multilayer coatings showed well-defined alternations between nitride and carbide layers, with morphology and crystallinity strongly influenced by ion energy and metal ion flux. The structural analysis confirmed the dominance of cubic solid solutions based on WNbN and WNbC, with minor hexagonal W_2N and Nb_2N detected. Grain sizes ranged from 6 to 15 nm, depending on deposition parameters. Optimal structure was achieved at moderate bias (–120 V) and high W arc current, yielding uniform layers, balanced composition, and enhanced crystallinity. The results demonstrate how controlled process parameters enable the design of high-performance nanocomposite coatings with tunable microstructure and phase composition, suitable for protective applications.
Keywords: *Multilayer coatings; Nitrides; Carbides; Niobium; Tungsten; Microstructure; Composition*
PACS: 68.55.Jk, 68.65.Ac

INTRODUCTION

To improve the quality, durability, and performance of metal products, various options are employed to alter their bulk structure and phase state while also modifying the surface for strengthening, enhancing thermal stability, and mitigating corrosion or friction. One of the most common and advanced methods for ensuring the desired operational properties of metal product surfaces is the application of functional films and coatings. Utilizing coatings increases the chemical stability of products and enhances mechanical and other properties, which significantly impacts their performance and service life, particularly under challenging conditions (thermobaric loads, friction, chemically active environments, etc.).

Among the various functional coatings, a distinct category consists of those designed to protect and enhance the operational qualities of cutting tools. Numerous cutting operations are prevalent in metalworking technologies across various sectors of mechanical engineering and other industries. The wear and premature failure of cutting tools pose a significant challenge, as they directly influence the efficiency and cost-effectiveness of their use, service life, and machining accuracy.

Among several methods for forming functional coatings, physical and chemical deposition technologies hold a significant position, particularly plasma technologies, which include processes like vacuum-arc evaporation or magnetron sputtering of metal targets and the deposition of condensate films. By adjusting the technological parameters of deposition (such as the composition of cathodes-evaporators, vacuum or gas environment, displacement potential on the substrate, geometry of the evaporators and substrates, and dynamic or static modes), it is possible to regulate the structural and phase state as well as the structure and architecture of coatings.

Protective two-element (binary) coatings of the first generation based on nitrides and carbides of titanium and zirconium (or those containing these compounds) have found widespread application due to properties such as high hardness, strong adhesion to the base, and resistance to wear, oxidation, and corrosion. Thus, coatings with TiC particles protect various components of mechanical systems [1], significantly increasing the wear resistance and hardness of parts. Coatings with TiN nitride are employed to modify and strengthen steel products [2, 3]. Zirconium nitride films are characterized by extraordinary overall stability, with excellent thermal and mechanical properties, high chemical inertness, and wear resistance, making them attractive for protecting a wide range of materials [4-6]. Alongside high hardness, toughness, and Young's modulus, niobium carbide (NbC) possesses an extremely high melting point, enabling the creation of coatings that provide material protection in high-temperature environments [7-10].

Cite as: O.V. Maksakova, V.M. Beresnev, S.V. Lytovchenko, D.V. Horokh, B.O. Mazilin, I. Afanasieva, M. Čaplovičova, M. Sahul, East Eur. J. Phys. 2, 297 (2025), https://doi.org/10.26565/2312-4334-2025-2-37

The aforementioned coatings have also found application in protecting cutting tools [11, 12], yet it became evident that binary nitride and carbide coatings have significant disadvantages, specifically low fracture toughness, high brittleness, and a tendency for microcrack formation [13]. This prompted the search for new methods to develop wear-resistant coatings that meet high standards of both hardness and strength.

One of these methods involves adding specific metals to binary compounds based on Ti, Nb, and Zr, resulting in the formation of ternary coatings with enhanced performance characteristics [14]. For instance, in [15], calculations of the microproperties of carbides (NbM)C, where M = V, Mo, W, and Cr (stability, mechanical parameters, and bonding structures) were conducted, demonstrating that the incorporation of V, Mo, W, and Cr atoms increases the hardness of carbides and reduces the mismatch between them and the matrix. The addition of TiC to WC [16] produces a significant hardness increase (> 3500 VHN) with nearly zero porosity, and its high melting point enables the use of such material in developing high-temperature resistant thermal protective coatings. The impact of molybdenum alloying on the microstructure and mechanical properties of transition metal carbides and nitrides for further enhancing the characteristics of these hard but brittle materials is illustrated by the examples of the compounds $(Nb_xMo_{1-x})C$ [17] and M_3Mo_3N and M_2Mo_4N (M = Fe, Co, Ni) [18]. Triple thin films based on nitrides, particularly TiMN, where M=V, Al, Mo, Cu, Mg, Zr, provide a combination of high hardness and wear resistance in coatings, a low coefficient of friction, and adequate corrosion protection compared to binary nitride compounds [19] [20]. The requirements of modern technology and industry for coating strength have led to the development of a new stage in improving coating quality: the creation of multilayer coatings, whose hardness often exceeds the individual hardness of the materials involved [21-23]. Many theoretical works are dedicated to explaining this phenomenon [24-26], which explore various mechanisms that lead to a significant increase in the hardness and strength of multilayer coatings compared to monolayer ones. Generally, hardness increases with a greater number of layers and a decreased thickness until reaching a maximum value in the nanometer range. For example, multilayer TiCN/TiNbCN coatings exhibit a direct relationship between an increase in the number of bilayers and a decrease in residual stress, along with changes in mechanical properties and fracture toughness [27]. In addition to improved strength, hardness, and wear resistance, the use of multilayer coatings addresses the issue of compatibility – meeting fundamentally different requirements for the part on one hand and for the coating/substrate on the other. It is challenging to satisfy these conflicting requirements with a single-layer coating, unlike a multilayer coating system [28].

The combination of carbide and nitride compounds in nanoscale multilayer coatings represents a scientifically compelling and practically valuable research direction. Previous studies, such as those involving TiN/SiC multilayers, have demonstrated that alternating nanoscale layers of two distinct ceramic phases can achieve superior hardness and wear resistance compared to their monolithic counterparts of equal total thickness [29]. This performance enhancement stems from the superlattice effect, interface strengthening, and restricted dislocation motion across compositional boundaries. Extending this concept to tungsten-based systems, which are less explored yet highly promising, introduces a new level of novelty. Tungsten nitride (WN) offers excellent thermal stability and hardness, while tungsten carbide (WC) is renowned for its wear resistance and oxidation tolerance at elevated temperatures. The integration of these two phases into a multilayer architecture could result in a universal protective material applicable across diverse industrial domains, including aerospace, energy, cutting tools, and electronics. Evidence from related systems supports this potential. In [30], Ti-WN/Ti-WC multilayers exhibited the lowest corrosion rate and the highest dielectric response when structured as high-period (n = 40) multilayers, confirming that finely tuned layer stacking significantly enhances performance. Furthermore, the synthesis of superlattice nc-TiN/a-$(W,Ti)C_{0.83}$ nanocomposites demonstrated superhardness, reduced friction, and outstanding high-temperature wear resistance [31].

Given these insights, multilayer coatings that combine tungsten-based nitrides and carbides present a novel and underexplored class of materials [32]. Their potential for tailoring mechanical, tribological, and electrochemical properties through structural engineering, such as alloying with elements from the group IV-VI, on a nanoscale, makes them an exciting frontier in advanced coating technologies. Investigating such systems will fill a knowledge gap in current materials science and open pathways to designing next-generation coatings for extreme environments. Utilizing the vacuum-arc PVD technique with a recently developed two-channel control device – "evaporator-injector," we have successfully synthesized carbide/nitride multilayer coatings based on W and Nb in a dynamically changing atmosphere of nitrogen and acetylene gases [33]. We reported on the deposition strategy of the multilayer with nanometer layer thicknesses and preliminarily assessed the microstructure, proving the formation of nanoscale multilayer coatings on a stainless-steel substrate.

This study investigated the structural and compositional evolution of monolayer WNbN and multilayer WNbN/WNbC coatings, deposited using cathodic arc evaporation (CAE-PVD). The influence of key deposition parameters – specifically the substrate bias voltage (–50 V to –200 V) and cathode arc current (130 – 150 A for W and 110 – 120 A for Nb) – was systematically explored. This work emphasized how controlled process tuning can be used to tailor the microstructure, phase constitution, and elemental distribution of these coatings, paving the way for multifunctional applications in demanding environments such as cutting tools or plasma-facing components.

EXPERIMENTAL DETAILS

Substrate Preparation

The main goal of preparing the substrate is to enhance its receptiveness to the coating layer, which is crucial for effective interfacial bonding. This process includes steps to remove contaminants from substrate preprocessing and

address surface defects through proper profiling. Figure 1 vividly depicts the sequence of these essential processes, highlighting their importance in achieving a superior finish.

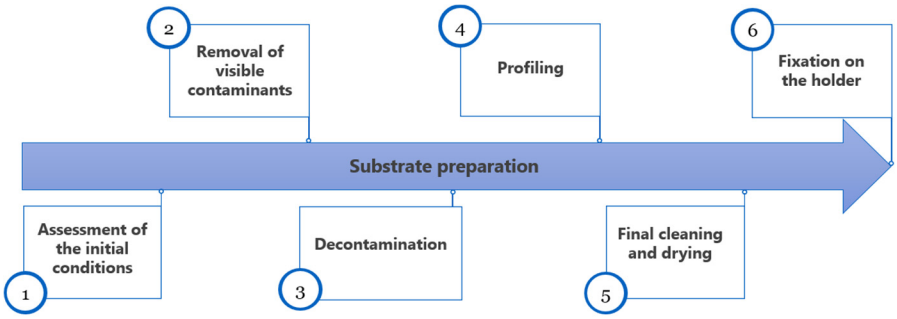

Figure 1. Steps for preparing substrates for coating deposition via the CAE-PVD method

Initially, an evaluation of the surface condition of the substrate was conducted to identify the presence of visible loose oxide layers, such as metallic rust species commonly found in tool steels, as well as dust particles and organic contaminants. Any accumulated dust was effectively eliminated using air blowing techniques. Subsequently, the substrate underwent a decontamination procedure, which is specifically designed to eliminate various contaminants, including grease, oils, chlorides, oxides, and hydrocarbons, from the substrate's surface. The presence of these contaminants, even in trace amounts, can significantly impair both the adhesion of coatings and the resultant properties of the substrate. The decontamination of the substrate was performed utilizing ultrasonic cleaning processes with alcohol. It is pertinent to note that even with the use of high-purity decontaminants, it remains impossible to achieve a completely contaminant-free substrate, primarily due to the existence of oxygen-containing species within the atmosphere. These oxide contaminants possess elevated surface energy and have a tendency to absorb additional contaminants with lower energy levels, particularly hydrocarbons, as a mechanism to reduce their surface energy. Nevertheless, these contaminants were subsequently removed through an etching process prior to the deposition of the coating. Figure 2 illustrates a typical decontamination process of the substrate surface prior to its fixation on the holder inside the deposition chamber.

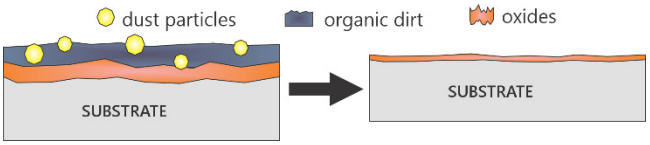

Figure 2. Decontamination process of the substrate surface for coating deposition via the CAE-PVD method

The subsequent step involves profiling the decontaminated substrate. This phase is critical in determining the degree of mechanical interlocking and chemical bonding of the coating to the substrate. The profiling of the substrate was accomplished through mechanical grinding and polishing methodologies. It utilized SiC grinding papers and polishing with a suitable medium, such as diamond suspensions with different particle sizes. Consequently, the resulting substrate profile was contingent upon the grit size of the SiC papers and the particle size of the polishing media. Mechanical profiling primarily focuses on achieving a face profile with minimal surface defects, including micro-cracks. Furthermore, it is imperative to exercise caution to prevent the induction of additional residual stresses in the substrate, as these can adversely affect the adhesion of the coating. Upon completion of substrate profiling, it is necessary to perform an additional cleaning of the substrates to remove any contaminants from the profiling process. The ultrasonic cleaning with a detergent, followed by thorough rinsing with deionized water, were applied. Finally, ensuring the substrate was dried before coating deposition is of utmost importance to mitigate the formation of pinholes.

Deposition Process

The series of operations involved in the deposition of coatings via the CAE-PVD method is illustrated in Figure 3. A comprehensive understanding of the sequence of processes and the principles underlying the deposition technique is crucial for enhancing coating quality and optimizing the resultant tribological performance. The process was initiated by loading appropriately prepared substrates into the deposition chamber. The distance maintained between the cathodes and substrates was 250 mm, thereby minimizing the impact of radiant heating during the evaporation process. Subsequently, the ramp-up stage commenced. It involved the preparation of the vacuum chamber for the cleaning process, elevating the temperature, and ultimately proceeding to the deposition stage. The chamber evacuation is imperative to inhibit gaseous contamination during the coating deposition. Consequently, a vacuum range of ($10^{-3} \div 10^{-4}$) Pa was established within the chamber. This stage was succeeded by heating to temperatures reaching 500 °C, serving as a precursor to the etching process.

The pre-treatment stage involved the removal of substrates' contaminants, which may be present, through a process known as plasma etching, where ions are utilized for bombardment. During the etching and subsequent coating deposition

stages, it is imperative to rotate the substrates to ensure uniformity in these processes. The primary objective of the etching procedure is to eliminate residue contaminants resulting from the decontamination process. This etching was executed using metal ion plasma. In this context, a high-speed plasma comprising metal ions from the targets was directed towards a highly negatively biased substrate (1000 V) for 5 minutes. This procedure induced the sputtering of surface contaminants and activated a superficial layer on the substrates' surfaces. The heating applied during this process is intended to facilitate the transport of etching species. At the same time, the high substrate biasing promoted the sputtering of surface contaminants and prevented the incorporation of the etching species within the substrate. In addition to decontamination, this process also led to roughening the substrate's surface, thereby enhancing the interlocking between the coating and the substrate. Following the etching process, the evacuation of gaseous contaminants occurred, and the vacuum conditions were re-established in preparation for the deposition of the coatings.

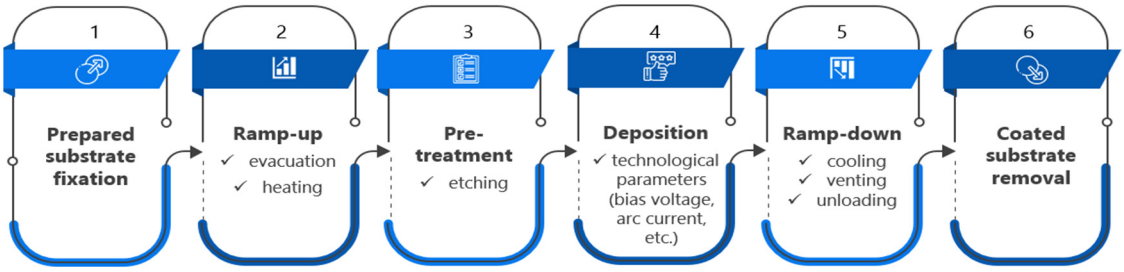

Figure 3. Operations in coating deposition via the CAE-PVD method.

Figure 4 illustrates the configuration of the CAE-PVD unit employed for deposition the coatings in this study. The monolayer and multilayer coatings were deposited by alternating technological parameters, as shown in Table 1. The deposition process was initiated with the evaporation of coating atoms from the target, achieved by initiating an arc on the cathode. The arc initiation was facilitated through a trigger arc generated by applying high voltage to an auxiliary electrode, which is typically positioned near the cathode surface. The behavior of the arc was influenced by various properties of the cathode, including its geometry, material composition, and purity level. Concentrated on the surface of the cathode, the generated arc gave rise to non-stationary micro-spots, referred to as cathode spots, on the target.

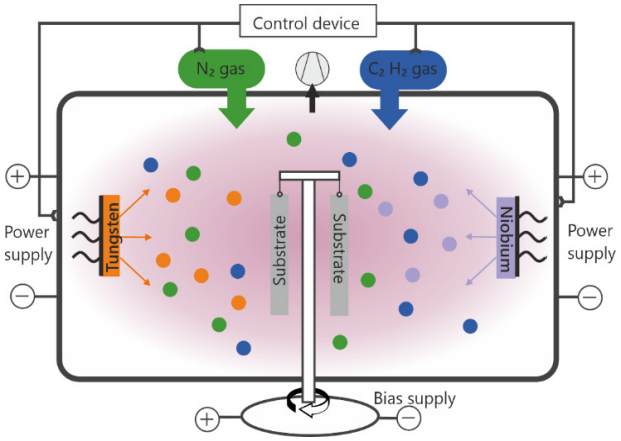

Figure 4. Schematic representation of the CAE-PVD unit used for coating deposition

Table 1. Deposition parameters of the experimental coatings.

Cathodes material	Substrate material	Coating	Arc current I_d, A	Bias voltage U_b, V	Gas composition	Gas pressure P, Pa
W 99.97 wt. % Nb 98.2 wt. %	12X18H9T (15 × 15 × 2.5 mm)	1-WNbN/WNbC	130/120	–200	N_2/C_2H_2	0.4
		2-WNbN/WNbC	150/110			
		3-WNbN/WNbC	150/115	–120		
		1-WNbN	120/90	–200	N_2	
		2-WNbN	130/130	–100		
		3-WNbN	130/120	–50		

The elevated current density observed at the cathode spot induces erosion, resulting in localized melting, ionization, and evaporation of the cathode materials. The reactive gases, namely nitrogen and acetylene, introduced into the deposition chamber, underwent activation by the plasma, leading to their dissociation into ions and additional electrons. Subsequently, the plasma was transported to the substrate. The particles within the plasma traversed at varying velocities,

contingent upon their atomic mass and energy. Upon reaching the surface of the substrate, the plasma volume adjacent to the substrate experienced a depletion of plasma species. Due to the superior mobility of electrons, they were lost at a comparatively accelerated rate, consequently establishing a potential difference between the substrate and the plasma. This phenomenon necessitated the implementation of a negative substrate bias to expedite the acceleration of positive coating ions toward the substrate, thereby enhancing the deposition rate. Following this process, the plasma species condensed onto the surface of the substrate. The ramp-down stage followed this. It entailed cooling and the safe unloading of the machine, ensuring that neither the film nor the desired substrate hardness was compromised. Furthermore, the chamber required cooling facilitated by cold water. Ultimately, the coated substrates were removed from the deposition chamber, and venting was employed to restore the vacuum chamber to ambient pressure.

RESULTS

Microstructural Evolution

Understanding the microstructural evolution processes in coatings deposited by the CAE-PVD method is crucial for enhancing tribological performance. This process begins with mobile coating atom species, known as adatoms, condensing on the substrate surface, leading to nucleation, nuclei growth, the establishment of the "coating–substrate" interface, and ongoing film growth. Figure 5 illustrates these stages. Initially, adatoms condense on the substrate surface. During this condensation, the adatoms lose energy from colliding with others, forming chemical bonds with the substrate's surface atoms, or impacting adatoms already bonded to the substrate. Preferential sites for incoming adatoms typically include surface defects or impurities. At this phase, the movement of adatoms is primarily influenced by bond strength. After condensation, nucleation occurs, with each condensing adatom acting as a site for further coating growth. The nucleation of coating atoms is significantly affected by the substrate's crystal structure, binding energy of adatoms, contaminants, and surface profile. Following nucleation, the growth of nuclei involves bonding between formed nuclei and incoming adatoms or pre-existing condensed adatoms via surface diffusion. This growth results in the creation of randomly oriented islands, which subsequently coalesce to form the interfacial region.

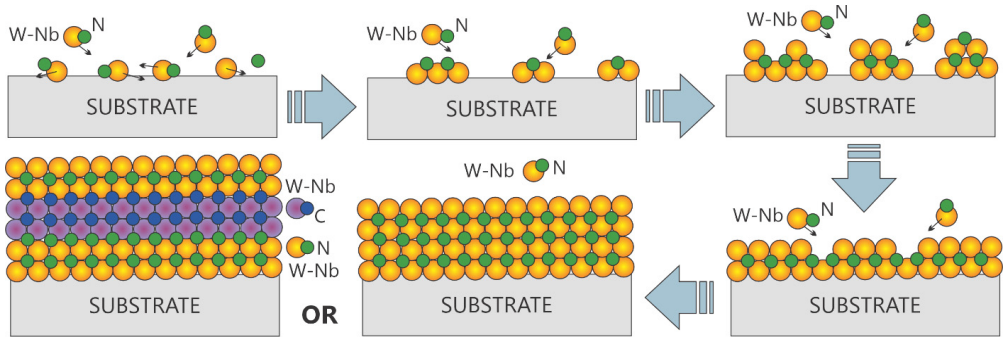

Figure 5. Schematic diagram depicting the microstructural evolution during the formation of the coatings via CAE-PVD method: adatom condensation → nucleation → nucleus growth → interface development → continuous film formation

Subsequent to the formation of the interface, the phase of continuous film growth commenced. This phase is characterized by the ongoing nucleation of the condensing adatoms at the interface, accompanied by perpetual growth, wherein previously deposited coating species are consistently enveloped by incoming ones. Throughout this process, grain coarsening occurs, as evidenced by the coalescence of the islands. The primary impetus for the migration of island boundaries is the imperative to minimize edge and surface energies, whereby islands with lower energy densities assimilate those with higher densities. This process is highly competitive, as crystallographic planes exhibiting higher densities are favored, resulting in accelerated growth compared to less dense planes. The disparity in growth rates among various crystallographic planes engenders a nonuniform coating surface morphology, thereby contributing to the increased surface roughness of the deposited coating. This phenomenon is particularly pronounced when the flux of incoming adatoms is oblique or when the adatoms possess low energy. Under these specific conditions, the influence of geometric shadowing becomes significantly pronounced, with the peaks of the rapidly growing planes capturing the entirety of the incoming adatoms, consequently overshadowing the valleys of the slower-growing planes. The resultant microstructure of the experimental coatings is illustrated in Figure 6 and Figure 7.

Figure 6 showcases the cross-sectional views of the monolayer WNbN coatings. The high-resolution images reveal a periodic nanostructure, which may arise from several contributing factors. The first factor pertains to the substrate rotation mode occurring in front of the two cathodes (W and Nb), resulting in alternating W and Nb fluxes during the deposition process. This behavior engenders periodic variations in composition (W-rich ↔ Nb-rich), even within a single monolayer deposition run. The second factor relates to limited interdiffusion, which is attributed to the low substrate temperature. Cathodic arc deposition typically transpires at moderate substrate temperatures. The restricted thermal diffusion inhibits the complete mixing of W and Nb layers during deposition, thereby preserving the compositional modulations resulting from the rotation cycles. This phenomenon further enhances the appearance of a “pseudo-multilayer” structure, despite the deposition being technically classified as monolayer. The third factor involves

high ionization and directionality. During CAE-PVD process, metal ions impinge upon the substrate with high energies and directed patterns. This characteristic can amplify the effects of angular flux discrepancies caused by rotation, contributing to the oscillating composition as deposition progresses. Conversely, SEM observations disclosed noticeable alterations in the microstructure of the WNbN coatings corresponding to decreases in substrate bias voltage. At the lowest applied bias of –50 V, the coating exhibits a distinctly layered structure characterized by sharp and well-defined interfaces, which remain discernible even at relatively low magnification. Columnar features are not prominent, and there is an absence of macroparticles or defects. At this reduced bias voltage, ion bombardment is minimized, resulting in decreased damage and intermixing. This environment facilitates the development of a highly ordered and periodic nanostructure, albeit with reduced density, culminating in a total thickness of 4.4 microns. As the bias voltage was elevated to –100 V, the coating exhibited moderate density accompanied by a smoother periodic nanostructure devoid of visible defects. The emergence of columnar growth was not observed. Re-sputtering effects began to affect the net deposition rate, culminating in a coating thickness of 2.3 microns. At the highest applied bias of –200 V, the morphology of the coating revealed a relatively dense and compact structure with fine, featureless contrast in the low-magnification image, indicative of high atomic packing density. The intense ion bombardment at this bias supplied sufficient energy to facilitate continuous re-nucleation and surface reorganization, resulting in enhanced packing density and superior structural cohesion. However, this energetic environment also induced significant re-sputtering of lighter elements, such as nitrogen, which diminished the overall deposition rate. Consequently, the final observed coating thickness was 3.2 microns. The interface between the coating and the substrate appeared sharply defined due to enhanced surface activation and improved adhesion under conditions of high-energy ion irradiation.

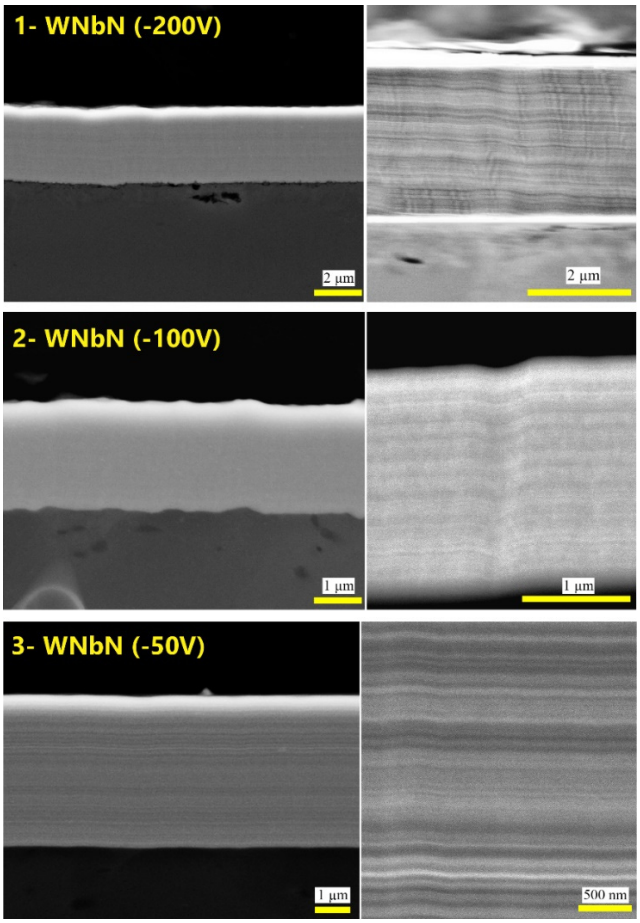

Figure 6. The cross-section structures of the monolayer WNbN coatings

Figure 7 illustrates the images depicting the surface morphology and cross-sectional architecture of the multilayer WNbN/WNbC coatings. All coatings demonstrate well-defined multilayer structures, which indicate successful modulation between the WNbN and WNbC layers. The periodicity and continuity of the layers were maintained under all deposition conditions, despite variations in arc current and bias voltage. The implementation of substrate rotation facilitated consistent deposition coverage and minimized shadowing effects. In the case of the multilayer 1-WNbN/WNbC coating, the surface reveals a relatively rough texture. The presence of structural defects such as cracks or delamination is not prominent, suggesting acceptable coating adhesion. While the multilayer architecture is discernible, it is less regular compared to alternative coatings. The total thickness of the multilayer region is approximately 423 nanometers. Some localized intermixing at the interfaces may be attributed to the lower W cathode current and the elevated Nb content. The

application of a higher bias voltage (–200 V) results in a denser structure but an increase in surface roughness due to intense ion bombardment and re-sputtering effects. In contrast, the multilayer 2-WNbN/WNbC coating exhibits a smoother surface than the previous coating, with fewer surface defects. This may be ascribed to the higher W cathode current, which promotes ionization and deposition uniformity. A highly regular multilayer structure is observed, with distinctly defined alternating layers and a total measured thickness of approximately 855 nanometers. The interfaces between the layers are sharper, indicating enhanced phase separation between nitride and carbide phases. The elevated W current of 150 A, in conjunction with intense ion bombardment, encourages a columnar, compact structure characterized by well-formed layer periodicity. This implies improved kinetic energy and momentum transfer during the alternating deposition cycles. The multilayer 3-WNbN/WNbC coating exhibits a refined structure characterized by large polygonal salients observable across the surface. The formation of droplets is less conspicuous, and the surface presents a more compact and smooth appearance, signifying diminished ion-induced surface damage attributed to the reduced bias voltage of –100 V. A distinctly ordered multilayer structure is apparent, with well-defined layer boundaries and a total measured thickness of approximately 583.5 nm. The layers appear thinner and more uniform, indicating controlled deposition occurring under moderate ion energies. The reduction in bias voltage from –200 V to –100 V leads to diminished re-sputtering and more precise layer formation. The elevated tungsten content, resulting from the 150 A arc current, is anticipated to slightly exceed that of niobium, while the structural modulation remains periodic and stable.

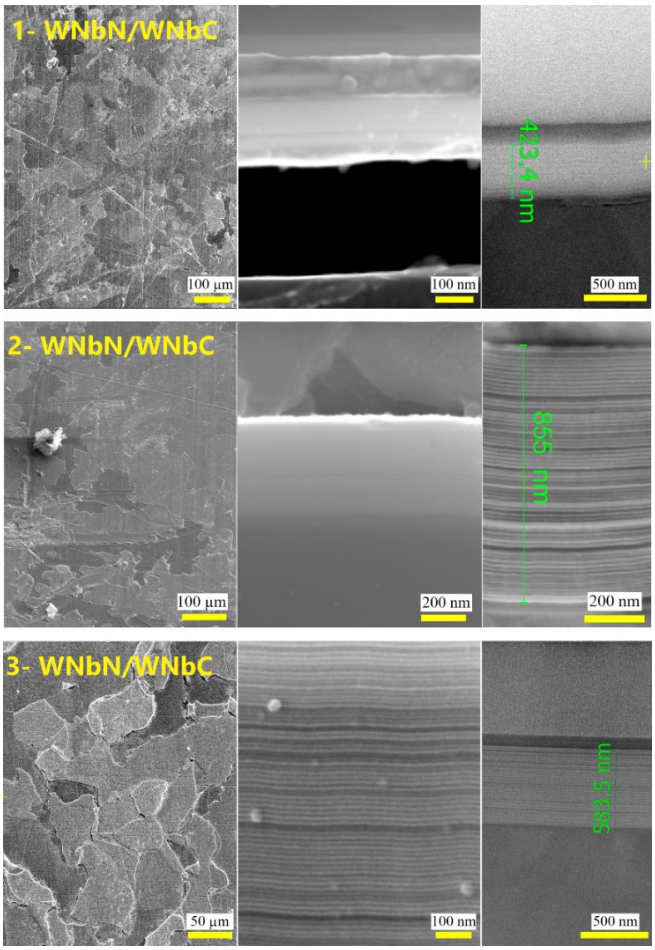

Figure 7. The surface and cross-section structures of the multilayer WNbN/WNbC coatings

These observations emphasize the critical importance of substrate bias in modulating the microstructural evolution of monolayer WNbN and multilayer WNbN/WNbC coatings during the CAE-PVD deposition. Adjusting the ion energy makes it feasible to attain an optimal equilibrium between coating density, grain refinement, and stoichiometry, achieving targeted functional performance.

Elemental Composition

The elemental composition of the multilayer WNbN/WNbC coatings is significantly influenced by the deposition parameters utilized during the CAE-PVD process. Comparative diagrams illustrating the elemental concentration in the multilayer WNbN/WNbC coatings are presented in Figure 8. It is apparent that the relative abundance of nitrogen in relation to carbon within the multilayer structure is primarily dictated by the ion bombardment energy, which is influenced by the substrate bias voltage.

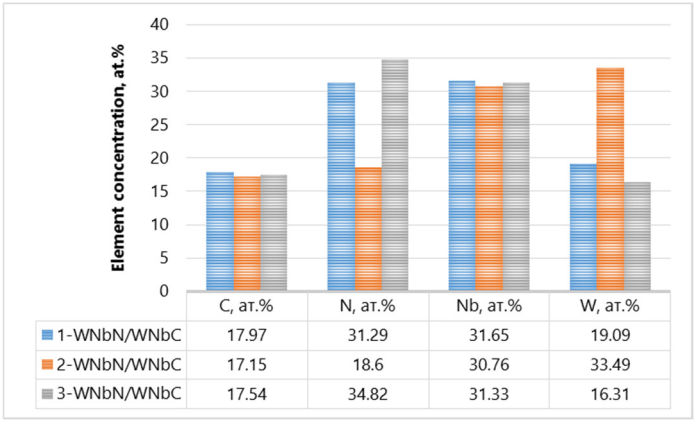

Figure 8. Elemental concentration diagrams of the multilayer WNbN/WNbC coatings

At an elevated bias voltage of –200 V, the increased ion energy facilitates the re-sputtering of lighter elements such as nitrogen and carbon. Although nitrogen atoms possess a lower atomic mass and higher volatility compared to carbon, rendering them more prone to re-sputtering, the deposition duration for the nitride layer was substantially longer than that for the carbide layers (N_2 = (55 ÷ 90) s, C_2H_2 = (5 ÷ 10) s). Consequently, under these conditions, it is anticipated that nitrogen will dominate over carbon in the multilayer structure. Upon the reduction of the bias voltage to –120 V, there is a notable decrease in the intensity of ion bombardment, which facilitates an enhanced retention of nitrogen, especially within the WNbN layers. Consequently, although carbon is anticipated to be more predominant overall, the relative nitrogen content is expected to rise as the bias voltage decreases as a result of diminished re-sputtering losses.

The relative concentrations of tungsten (W) and niobium (Nb) are significantly affected by both their respective arc current settings and inherent properties, including atomic mass and ionization efficiency. At an elevated arc current of 150 A for the W cathode, as opposed to 130 A, the W ion flux exhibits a substantial increase, facilitating elevated tungsten deposition rates. Concurrently, the arc current applied to the Nb cathode is comparatively lower, either 110 A or 120 A, which diminishes the niobium ion density within the plasma. Notably, the observed Nb concentration is remarkably high, ranging from 30.76 to 31.65 at. %, in relation to W (16.31 and 19.09 at. %). This phenomenon can be explicated by two principal factors: increased macroparticle emission and the interplay of tungsten's ionization energy and ion charge states. The first factor posits that the W cathode is recognized for its propensity to emit a greater volume of macroparticles (i.e., droplets) owing to its higher melting point and unique vaporization behavior. These macroparticles typically fail to integrate into the developing coating and may adhere to the chamber walls or accumulate within the system, consequently resulting in a net depletion of W content in the deposited coating when juxtaposed with Nb. The second factor underscores that tungsten possesses a higher ionization energy than niobium; in cathodic arc scenarios, this disparity can lead to a reduced fraction of multiply charged W ions. Consequently, Nb ions, being less heavy and more readily ionized, may prevail in the plasma and reach the substrate with greater efficiency, particularly when the substrate bias applied is insufficient to attract the heavier, less mobile W ions.

A trade-off outcome is observed for the multilayer 2-WNbN/WNbC coating. The tungsten ions possess greater mass and momentum, resulting in a higher probability of incorporation into the film, particularly under elevated substrate bias conditions of –200 V, which increases ion impact energy. This advantage is further enhanced by the higher arc current applied to the tungsten cathode. Consequently, under both bias conditions, especially at –200 V and an arc current of 150 A, tungsten (33.49 atomic percent) predominates over niobium (30.76 atomic percent) in the coating composition.

The elemental composition of monolayer WNbN coatings was found to be significantly affected by the applied substrate bias voltage. Monocoatings were deposited in a rotational substrate mode using dual metallic cathodes (tungsten and niobium) in the presence of nitrogen as the reactive gas. The substrate bias voltage was varied between -200 V, -100 V, and -50 V to examine its influence on the resulting coating composition. Comparative diagrams illustrating the elemental concentration in the monolayer WNbN coatings are shown in Figure 9.

At a higher bias voltage of –200 V, the intensified ion bombardment led to substantial re-sputtering of lighter elements such as nitrogen and carbon from the coating surface. This phenomenon resulted in metal-rich coatings with a potential shift toward sub-stoichiometric compositions, particularly in nitrogen-deficient $WNbN_x$ phases. Although a higher substrate bias (–200 V) is typically associated with enhanced incorporation of heavier elements like tungsten due to increased ion momentum, the observed composition of the WNbN coating shows a higher Nb content. This discrepancy is likely attributed to a combination of factors, including the higher ion flux and better ionization efficiency of Nb under cathodic arc conditions, greater erosion rate of Nb cathodes, and possibly less efficient incorporation or greater re-sputtering of tungsten ions. Additionally, geometric factors such as substrate positioning and the relative plasma exposure during rotation may have further favored Nb accumulation. These effects, taken together, resulted in the Nb-rich WNbN coating despite the applied high bias voltage.

Upon the reduction of the bias voltage to –100 V, the re-sputtering effect diminished significantly, thereby enhancing the retention of nitrogen within the developing coating. This condition facilitated the formation of coatings that are closer

to stoichiometric compositions, characterized by a more balanced ratio of metal to nonmetal. The relative incorporation of niobium increased as the disparity in ion kinetic energies between tungsten (W) and niobium (Nb) decreased.

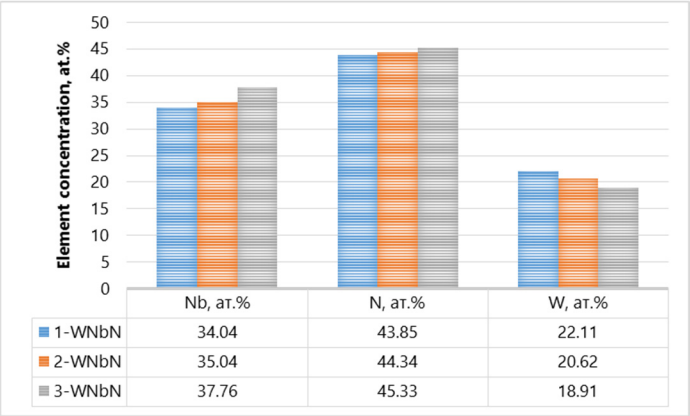

	Nb, ат.%	N, ат.%	W, ат.%
1-WNbN	34.04	43.85	22.11
2-WNbN	35.04	44.34	20.62
3-WNbN	37.76	45.33	18.91

Figure 9. Elemental concentration diagrams of the monolayer WNbN coatings

At the minimal bias voltage of –50 V, the bombardment of ions was reduced, leading to the highest levels of nitrogen incorporation across all examined technological conditions. Although this promoted nearly ideal stoichiometry, it concurrently heightened the risks associated with the over-saturation of the non-metallic element. In the case of WNbN coatings, this may result in the development of nitrogen-rich amorphous regions or secondary nitride phases. Furthermore, a decrease in the incorporation of tungsten was noted, attributed to the diminished contribution of heavy metal ions within this lower ion energy regime.

In summary, increasing the substrate bias voltage leads to metal-enriched coatings with higher Nb content and reduced nitrogen concentration, while lower bias values promote more stoichiometric compositions and higher niobium content. These compositional variations are expected to strongly influence the resulting structural properties of the coatings, as discussed in the abovementioned sections.

Phase Evolution

Figure 10 presents the X-ray diffraction patterns of the monolayer WNbN coatings. All diffraction patterns exhibit broad peaks in the 2θ range of 30° – 80°, indicating nanocrystalline or fine-grained structures.

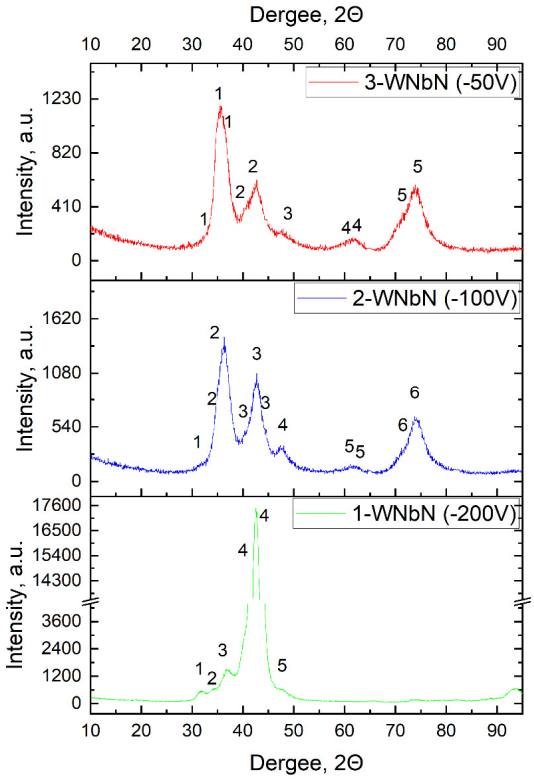

Figure 10. Diffraction patterns of the monolayer WNbN coatings

The most intense peaks are located around ~36.5 – 37° (2θ), ~42.5 – 43° (2θ), ~62.5 – 63° (2θ), and ~70 – 80° (2θ) (see Table 2). These peaks can be attributed to the face-centered cubic WNbN phase (NaCl-type structure), which is consistent with δ-WN (PDF #25-1257) and δ-NbN (PDF #38-1155). The presence of peaks in the range ~31.6 – 33.6° (2θ), ~46.8 – 47.4° (2θ), and ~60.38° (2θ) suggests the formation of minor hexagonal nitride phase W_2N and/or Nb_2N, which is consistent with hexagonal W_2N (PDF #25-1256) and hexagonal Nb_2N (PDF #17-0381).

Table 2. Peak list and identification for the monolayer WNbN coatings.

	Peak no.	Position 2θ (°)	Phase	Crystal System	Plane (hkl)	d-spacing
1-WNbN (–200 V)	1	31.77	W_2N / Nb_2N	hex	(100)	2.8136
	2	33.63	W_2N / Nb_2N	hex	(101)	2.6622
	3	37.01	WNbN solid solution (W-rich)	cubic	(111)	2.4266
	4	39.90	W_2N or Nb_2N	hex	(102)	2.2574
	4	42.50	WNbN solid solution (W-rich)	cubic	(200)	2.1252
	5	46.80	W_2N / Nb_2N	hex	(103)	1.9388
2-WNbN (–100 V)	1	31.64	W_2N / Nb_2N	hex	(100)	2.8250
	2	34.95	WNbN solid solution (Nb-rich)	cubic	(111)	2.5650
	2	36.37	WNbN solid solution (W-rich)	cubic	(111)	2.4680
	3	40.15	WNbN solid solution (Nb-rich)	cubic	(200)	2.2436
	3	42.60	WNbN solid solution (W-rich)	cubic	(200)	2.1204
	3	44.37	WNbN solid solution	cubic	(210)	2.0395
	4	47.45	Nb_2N / W_2N	hex	(104)	1.9144
	5	60.38	Nb_2N / W_2N	hex	(110)	1.5316
	5	62.01	WNbN	cubic	(220)	1.4955
	6	70.78	WNbN solid solution (Nb-rich)	cubic	(311)	1.3298
	6	74.00	WNbN solid solution (W-rich)	cubic	(311)	1.2798
3-WNbN (–50 V)	1	34.75	NbN	cubic	(111)	2.5793
	1	35.65	Nb_2N / W_2N	hex	(101)	2.5162
	1	36.90	WNbN solid solution (W-rich)	cubic	(111)	2.4338
	2	40.04	WNbN solid solution (Nb-rich)	cubic	(200)	2.2496
	2	42.40	WNbN solid solution (W-rich)	cubic	(200)	2.1299
	3	47.73	Nb_2N / W_2N	hex	(104)	1.9036
	4	60.35	Nb_2N / W_2N	hex	(110)	1.5323
	4	62.23	WNbN (solid solution)	cubic	(220)	1.4904
	5	70.32	WNbN solid solution (Nb-rich)	cubic	(311)	1.3375
	5	73.75	WNbN solid solution (W-rich)	cubic	(311)	1.2836

The substrate bias voltage is crucial in determining the crystalline quality and grain size of monolayer WNbN coatings obtained using CAE-PVD. The low bias of –50 V results in lower energy ion bombardment, leading to lower adatom mobility and less recrystallization, producing a fine-grained (nanocrystalline) structure of the monolayer 3-WNbN coating. The first broad peak with overlapping contributions in the region of 34.75°, 35.65°, and 36.9° (2θ) suggests the presence of multiple overlapping crystallographic planes from different phases or orientations. This is very common in nanocrystalline and multiphase nitride coatings, especially those produced by CAE-PVD. The peak at 34.75° (2θ) is assigned to the (111) plane of cubic NbN. It suggests the presence of Nb-rich cubic domains within the WNbN solid solution or a segregated cubic NbN phase forming at Nb-dominant growth points (due to arc rotation or target flux variation). The main peak at 35.65° (2θ) refers to hexagonal Nb_2N or W_2N with (100) reflection. The peak at 36.9° (2θ) corresponds to the (111) plane of cubic WN and suggests the W-rich domain in the WNbN solid solution. Another broad but less intensive peak centered around 40.04° and 42.4° (2θ) is a superposition of (200) reflections from both W-rich and Nb-rich regions in the cubic WNbN solid solution. The peak at ~40.04° (2θ) strongly refers to (200) reflection of cubic NbN or a region of the WNbN solid solution that is locally enriched in Nb. The peak at ~42.4° (2θ) is strongly assigned to the (200) reflection of cubic WN or W-rich region within the cubic WNbN solid solution. The peak at

47.73° (2θ) refers to minor hexagonal Nb_2N or W_2N (104), which may form in N-deficient regions. A broad and least intensive peak in the 60.3° to 62.2° (2θ) range is a key signature of overlapping reflections from cubic WNbN and potentially minor hexagonal nitride phases. The peak at 60.35° (2θ) is most likely hexagonal W_2N or Nb_2N (110). The peak at 62.23° (2θ) is strongly assigned to the cubic WNbN solid solution with (220) reflection. The broad peak between 70.32° and 73.75° (2θ) is a composite peak, most likely originating from overlapping reflections of cubic and hexagonal phases. The peak at 70.32° (2θ) refers to cubic NbN (311) or a Nb-rich region in the WNbN solid solution. The peak at 73.75° (2θ) corresponds to cubic WN (311) or a W-rich region in the WNbN solid solution.

The increase of bias voltage to –100 V causes a slightly higher ion bombardment, enhancing surface diffusion, promoting crystal growth, and increasing grain size. Therefore, the monolayer 2-WNbN coating formed with improved crystallinity with more defined peaks. The small peak positioned at 31.64° (2θ) indicates the formation of minor hexagonal W_2N or Nb_2N phases with (100) reflection. The main broad peak consists of two overlapping contributions in the region of 34.95° and 36.97° (2θ). The peak at 34.95° (2θ) strongly corresponds to cubic (111) WNbN solid solution enriched with Nb. The peak at 36.97° (2θ) refers to cubic (111) WNbN solid solution enriched with W. Another broad but less intensive peak centered around 40.15° and 42.60° (2θ) is a superposition of (200) reflections from both W-rich and Nb-rich regions in the cubic WNbN solid solution. The peak at 44.37° (2θ) is the (210) reflection of cubic WNbN solid solution, typical in highly oriented or dense coatings. The peak at 47.45° (2θ) refers to minor hexagonal Nb_2N or W_2N phases with (104) reflection. Its presence supports the presence of small amounts of secondary phases or that finer structural details are being resolved. A broad peak in the 60.38° to 62.01° (2θ) range is composed of the overlapping reflections from cubic and potentially minor hexagonal nitride phases. The peak at 60.38° (2θ) refers to the hexagonal W_2N or Nb_2N (110). The peak at 62.01° (2θ) is strongly assigned with cubic WNbN (220). The broad peak between 70.78° – 74.0° (2θ) refers to WNbN solid solution with (311) reflection, which is consistent with other major reflections (111), (200), (220), and broaden by the composition (Nb- and W-rich regions).

At high bias voltage of –200 V, the intense ion bombardment may cause the densification and possibly stress-induced recrystallization. It results in larger grains and sharper diffraction peaks. The extremely high intensity may also be influenced by preferred orientation effects (texture). The diffraction peak at ~31.77° (2θ) indicates the formation of hexagonal W_2N (or Nb_2N) as a minor phase in the monolayer 1-WNbN coating. These phases can both exhibit peaks in the 31 – 32° (2θ) range, specifically, W_2N (100) → ~31.6 – 31.8° (2θ) and Nb_2N (100) → ~31.5 – 31.7° (2θ), and may form as secondary or surface-stabilized phases in nitrogen-deficient regions, especially under high-energy deposition conditions typical for CAE-PVD process. The peak at 33.63° (2θ) also supports the earlier assumption of minor hexagonal phase presence with (101) reflection. The peak at 37.01° (2θ) is highly consistent with the (111) reflection of a cubic WNbN solid solution phase, where W and Nb are substitutional, and the lattice parameter lies between that of WN and NbN. The peak at 39.9° (2θ) refers to the presence of the hexagonal phase with (102) reflection. The main peak between at 42.5° (2θ) is the (200) peak of the cubic WNbN solid solution. The peak at 46.8° (2θ) assigned to hexagonal nitride with (103) reflection, supporting the presence of minor W_2N/Nb_2N phases.

Based on the (111)/(200) reflections at ~36.5° – 43° (2θ), a qualitative trend in grain size was estimated as follows. The monolayer 3-WNbN coating has the smallest grain size in the range of ~5 – 7 nm, the monolayer 2-WNbN coating has moderate grain growth with sizes of ~10 – 12 nm and the monolayer 1-WNbN coating has the largest grain size ranging between ~15–20 nm.

Thus, the monolayer 3-WNbN and 2-WNbN coatings strongly supports the presence of a cubic NaCl-type WNbN structure, with minor hexagonal contributions that may reflect local composition variation or grain boundary effects. The deposition of the coatings at low (–50 V) and moderate (–100 V) bias voltage results in nanocomposite structures of the coatings with nanocrystalline nitride grains (~5 – 12 nm). The monolayer 1-WNbN coating is dominantly cubic WNbN with bigger contributions from hexagonal phases, indicating possible formation of W_2N or Nb_2N in local regions – potentially from N-deficient zones, or interfacial effects during high-energy deposition. The increase of bias voltage to -200 V produce the grains growth to larger sizes of ~20 nm and formation of the strong texture.

Figure 11 presents the X-ray diffraction patterns of the multilayer WNbN/WNbC coatings. All diffraction patterns exhibit distinct broadening and overlapping peaks in the 2θ range of 30° – 80°, indicating the presence of nanocrystalline and multiphase structures. The most intense peaks are located at ~36 – 38° (2θ), 43 – 44.5° (2θ), 62–64° (2θ), and 70–80° (2θ) (see Table 3). The observed peaks can be ascribed to the cubic WNbN phase (NaCl-type structure), which aligns with cubic WN (PDF #25-1257) and cubic NbN (PDF #38-1155), along with the WNbC phase, which likely exhibits a cubic B1-type structure (cubic WC - PDF #89-2868 and cubic NbC - PDF #38-1364). Additionally, low-intensity or broad peaks located near 31.6°, 33.6°, and 37.0° (2θ) may suggest the existence of hexagonal W_2N and Nb_2N as secondary phases, corresponding with hexagonal W_2N (PDF #25-1256) and hexagonal Nb_2N (PDF #17-0381). This phenomenon is particularly pronounced for the 3-WNbN/WNbC coating obtained under reduced bias conditions, where diminished ion energy is conducive to mixed-phase formation.

Lower arc currents (130/120 A) and a high bias voltage (–200 V) facilitate the formation of fine grains through enhanced re-sputtering and densification processes for the multilayer 1-WNbN/WNbC coating. The peak occurring at 31.55° (2θ) is ascribed to the (100) reflection of hexagonal W_2N or Nb_2N, indicating the existence of under-stoichiometric nitride phases at specific interfaces or resulting from localized nitrogen deficiency during the deposition cycle. The peak observed at 35.69° (2θ) corresponds to the (111) reflection of cubic NbC or cubic WC, suggesting the development of

carbides during the acetylene-assisted segments of the deposition. Given the slightly lower W arc current in this sample, it is anticipated that the NbC contribution will predominate. A broad peak at 39.70° (2θ) is associated with the (111) plane of a cubic WNbN solid solution with a high Nb content, which embodies the predominant structure of the nitride layers. This NaCl-type phase is indicative of transition metal nitrides formed under energetic deposition conditions. The weak reflection at 42.95° (2θ) likely encompasses contributions from (200) reflection of cubic WNbN solid solution with a high W content, reinforcing the existence of the cubic nitride phase in conjunction with the (111) reflection. The broadness of the peak is attributed to nanocrystallinity. The peak at 44.75° (2θ) aligns with the (200) reflection of cubic NbC or WC phases, further supporting the formation of well-structured carbide layers. At 47.63° (2θ), the (200) reflection of minor hexagonal Nb_2N or W_2N phases with (104) reflection.

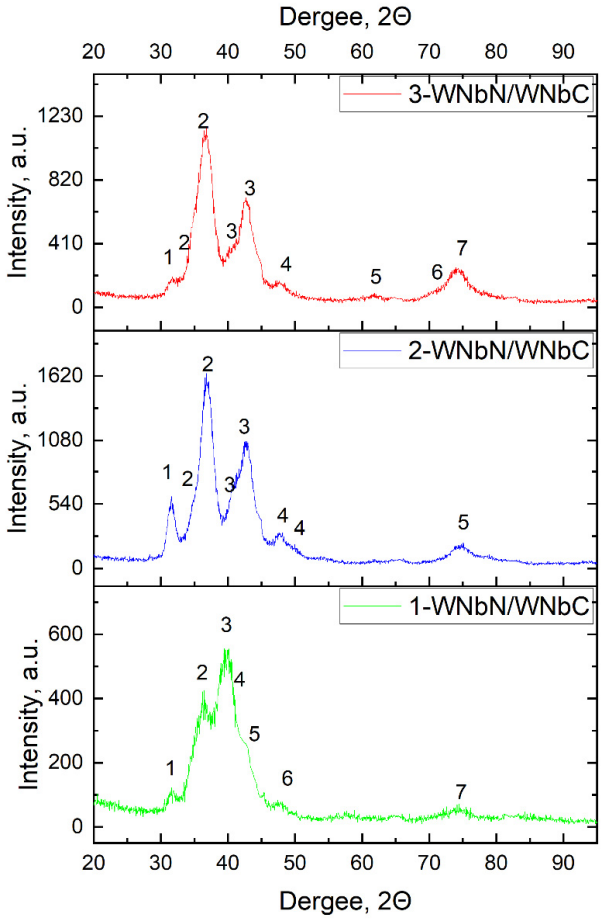

Figure 11. Diffraction patterns of the multilayer WNbN/WNbC coatings

The overall peak broadness indicates a nanocrystalline structure, with crystallite sizes estimated to be in the 6–8 nm range using the Scherrer equation. The relatively lower W arc current (130 A) may have contributed to a slightly reduced metal flux, which limits adatom mobility and suppresses grain growth. Meanwhile, the high substrate bias (–200 V) enhances surface densification and re-sputtering, promoting finer grain sizes and more uniform layer interfaces, albeit at the cost of increased compressive stress and peak broadening.

Table 3. Peak list and identification for the multilayer WNbN/WNbC coatings.

	Peak no.	Position 2θ (°)	Phase	Crystal System	Plane (hkl)	d-spacing
1-WNbN/WNbC	1	31.55	Nb_2N / W_2N	hex	(100)	2.8332
	2	35.69	NbC / WC	cubic	(111)	2.5135
	3	39.70	WNbN solid solution (Nb-rich)	cubic	(111)	2.2683
	4	42.95	WNbN solid solution (W-rich)	cubic	(200)	2.1041
	5	44.75	NbC / WC	cubic	(200)	2.0234
	6	47.63	Nb_2N / W_2N	hex	(104)	1.9074
	7	74.42	WNbN solid solution	cubic	(220)	1.2731

	Peak no.	Position 2θ (°)	Phase	Crystal System	Plane (hkl)	d-spacing
2-WNbN/WNbC	1	31.45	Nb_2N / W_2N	hex	(100)	2.8420
	2	34.50	NbC / WC	cubic	(111)	2.5973
	2	36.80	Nb_2N / W_2N	hex	(101)	2.4402
	3	40.60	WNbN solid solution (Nb-rich)	cubic	(111)	2.2201
	3	42.65	WNbN solid solution (W-rich)	cubic	(200)	2.1180
	4	47.64	Nb_2N / W_2N	hex	(104)	1.9071
	4	49.80	Nb_2N / W_2N	hex	(110)	1.8292
	5	74.47	WNbN solid solution	cubic	(220)	1.2729
3-WNbN/WNbC	1	31.75	W_2N / Nb_2N	hex	(100)	2.8150
	2	34.65	NbC / WC	cubic	(111)	2.5865
	2	36.65	Nb_2N / W_2N	hex	(101)	2.4498
	3	40.19	WNbN solid solution (Nb-rich)	cubic	(111)	2.2415
	3	42.55	WNbN solid solution (W-rich)	cubic	(200)	2.1228
	4	47.52	Nb_2N / W_2N	hex	(104)	1.9115
	5	61.63	WNbN	cubic	(220)	1.5034
	6	70.28	WNbN solid solution (Nb-rich)	cubic	(311)	1.3382
	7	74.15	WNbN solid solution (W-rich)	cubic	(311)	1.2776

An increase in tungsten arc current to 150 A coupled with a reduction in niobium arc current to 110 A for the multilayer 2-WNbN/WNbC coating results in the diffraction peaks becoming sharper and more intense. The peak observed at 31.45° (2θ) corresponds to the (100) reflection of hexagonal W_2N or Nb_2N. This peak is indicative of under-stoichiometric or early-stage nitride phases and suggests localized nitrogen-deficient growth, potentially occurring at nitride-carbide interfaces. The reflection located at 34.50° (2θ) likely arises from overlapping contributions from cubic WC or cubic NbC, corresponding to the (111) plane. The formation of these carbides is associated with the acetylene-assisted deposition stages and is enhanced by the elevated W arc current. The prominent peak centered around 36.80° (2θ) is attributed to the (101) reflection of hexagonal W_2N/Nb_2N, although contributions from W_2C cannot be dismissed. This region typically reflects overlapping nitride and carbide signals, particularly within nanostructured multilayers. A weak reflection at 40.60° (2θ) is ascribed to the (111) plane of the cubic WNbN solid solution enriched with Nb, representing the primary signature of a cubic NaCl-type structure, which is common to transition metal nitrides deposited by arc evaporation. The adjacent peak at 42.65° (2θ) can be indexed to the (200) reflection of the cubic WNbN solid solution, thereby confirming the continuity of the cubic nitride structure across multiple stack layers. The peak at 47.64° (2θ) corresponds to the minor hexagonal Nb_2N or W_2N (104), which may form in N-deficient regions. A reflection at 49.80° (2θ) is attributed to the (110) plane of hexagonal Nb_2N or W_2N, further corroborating the presence of hexagonal domains within the coating. These may develop in regions where nitrogen incorporation is kinetically limited or disrupted during gas switching. Lastly, the high-angle reflection at 74.47° (2θ) aligns with the (220) plane of the cubic WNbN solid solution. The discernibility of this peak, despite its typically low intensity, indicates a well-aligned and crystalline cubic nitride phase within specific domains of the multilayer.

The observed peak widths suggest a significant broadening characteristic of nanocrystalline materials. This broadening likely results from a combination of small grain sizes (estimated to be in the range of 10 – 12 nm according to the Scherrer equation), internal microstrain, and the complex chemical modulation intrinsic to multilayer architectures. The elevated arc current on the W cathode (150 A) enhances the flux of metal ions, facilitating denser and more crystalline growth, particularly within the carbide layers. Concurrently, the implementation of a high substrate bias (–200 V) promotes densification and restricts adatom mobility, thus suppressing excessive grain growth while simultaneously increasing compressive stress, which may induce a slight shift in peak positions.

The reduction of the bias voltage to –120 V results in a decrease in ion bombardment intensity, which subsequently limits re-sputtering and fosters grain growth, culminating in an enhancement of crystallinity within both nitride and carbide phases. A series of pronounced yet comparatively broad peaks were detected for the multilayer 3-WNbN/WNbC coating. Specifically, the peak positioned at 31.75° (2θ) is attributed to the (100) reflection of hexagonal W_2N or Nb_2N. This phase indicates under-stoichiometric nitride domains, which may develop during the initial stages of nitride layer formation or within areas of diminished nitrogen activity occurring between gas switching intervals. The reflection observed at 34.65° (2θ) correlates with the (111) or (101) planes of cubic NbC or WC, respectively. These phases typically emerge during the acetylene-assisted deposition phases, particularly under elevated metal ion flux conditions, as

facilitated by the increased W arc current. The peak recorded at 36.65° (2θ) corresponds to the (101) plane of hexagonal W_2N or Nb_2N, potentially overlapping with faint reflections originating from W_2C. Its presence further reinforces the coexistence of minor hexagonal phases, often more stable at lower ion energies. A prominent peak at 40.19° (2θ) aligns with the (111) reflection of the cubic WNbN phase, which characterizes a NaCl-type solid solution comprising WN and NbN. This peak signifies the primary orientation of the nitride phase within the multilayer stack. The peak at 42.55° (2θ) correlates with the (200) reflection of the cubic WNbN solid solution, thereby confirming the existence of a continuous and well-crystallized B1-type structure across the multilayers. The peak at 47.52° (2θ) is interpreted as the minor hexagonal Nb_2N or W_2N phase exhibiting a (104) reflection. The peak at 61.63° (2θ) constitutes a continuation of the cubic series, aligning with the (220) reflection of cubic WNbN (with minor contributions from WNbC), thereby reinforcing the observation of a predominant NaCl-type structure throughout the multilayer stack. The reflection noted at 70.28° (2θ) is attributed to the (311) plane of cubic NbN, suggesting the presence of Nb-rich domains within the WNbN solid solution layers or localized segregation resulting from slight fluctuations in plasma composition. Finally, the peak at 74.15° (2θ) corresponds to the (311) plane of cubic WN or WNbN, thereby further substantiating the establishment of a well-defined cubic structure and the existence of W-rich zones, potentially influenced by the relatively high W arc current.

The observed diffraction peaks exhibit greater breadth compared to those of bulk materials, while remaining sharper than those present in coatings deposited at increased bias voltages (e.g., 1-WNbN/WNbC and 2-WNbN/WNbC). This observation suggests a nanocrystalline structure characterized by enhanced grain growth, which is facilitated by the moderately diminished bias voltage (–120 V). The decrease in ion bombardment energy has permitted increased adatom mobility, subsequently leading to larger crystallite sizes and more distinct phase separation. The average crystallite size, as estimated utilizing the Scherrer equation, falls within the range of 10 – 15 nm.

The multilayer 1-WNbN/WNbC coating features a mixed-phase nanocrystalline structure primarily composed of cubic WNbN and NbC phases, with smaller amounts of hexagonal W_2N/Nb_2N. The deposition conditions lead to a dense, fine-grained multilayer with overlapping phase domains, resulting in a broad and diffuse XRD profile. The high bias voltage results in densification and stress-induced peak shifts, while moderate arc currents facilitate balanced phase formation throughout the multilayer stack. There is a minor presence of hexagonal phases. The multilayer 2-WNbN/WNbC multilayer coating combines cubic and hexagonal nitride phases. The dominant cubic WNbN and WNbC/NbC forms are substantiated by distinct (111), (200), and (220) reflections, while weaker peaks associated with hexagonal W_2N, and Nb_2N indicate minor phase segregation or localized composition variations. These findings highlight the intricate nature of phase formation in reactive arc-deposited multilayer systems and demonstrate how deposition parameters like arc current, reactive gas switching, and bias voltage affect structural evolution. An increased occurrence of hexagonal phase peaks suggests a reduced energy barrier for non-cubic phases. The multilayer 3-WNbN/WNbC coating displays a well-defined nanocrystalline multilayer structure, dominated by cubic WNbN and WNbC phases (NaCl-type structure), with minor hexagonal W_2N/Nb_2N phases. A moderate bias voltage (–120 V) and high W arc current enhanced grain growth, crystallinity, and phase stability while limiting excessive re-sputtering and decreasing structural defects. There is a minor presence of hexagonal phases. These properties render this coating the most crystalline and structurally coherent among the three WNbN/WNbC multilayer systems studied.

CONCLUSIONS

This study explores the microstructural, compositional, and phase evolution characteristics of both monolayer WNbN and multilayer WNbN/WNbC coatings, which were deposited via cathodic arc evaporation under different process conditions. Three distinct monolayer WNbN coatings and three multilayer WNbN/WNbC coatings were synthesized utilizing dual-metallic cathodes (W and Nb), with nitrogen and acetylene serving as reactive gases. The essential deposition parameters, namely substrate bias voltage and cathode arc current, were methodically altered to investigate their impact on the coating structure, morphology, elemental distribution, and phase composition.

The microstructural analysis of monolayer WNbN coatings demonstrates a significant effect of substrate bias voltage on their evolution during cathodic arc evaporation. A clear pseudo-multilayer structure was observed in all samples, resulting from the interactions between substrate rotation, angular deposition flux from dual cathodes, and limited interdiffusion at moderate deposition temperatures. With low bias (–50 V), the coatings showcased distinct periodic layering, exhibiting minimal columnar growth and high structural order, although with lower density. As the bias increased to –100 V and –200 V, the morphology transitioned to denser, more compact structures, with the highest bias facilitating continuous re-nucleation, enhanced atomic packing, and improved interfacial adhesion. However, higher ion energies led to marked re-sputtering effects, which diminished net deposition rates and slightly affected stoichiometry. These findings underscore the pivotal role of bias voltage in balancing coating morphology, density, and composition – a vital element for optimizing monolayer WNbN coatings for advanced functional uses.

The characterization of multilayer WNbN/WNbC coatings at the morphological and microstructural levels confirmed the effective creation of periodic multilayer structures. The coatings displayed clear alternations between nitride and carbide layers, achieved through substrate rotation and precise gas pulsing. Factors such as arc current and bias voltage impacted layer definition, thickness uniformity, and the sharpness of interfaces. With a –200 V bias, the multilayer 1-WNbN/WNbC and 2-WNbN/WNbC coatings exhibited denser microstructures, though the multilayer

1-WNbN/WNbC had increased surface roughness and interfacial intermixing attributed to a lower W arc current (130 A). Conversely, the multilayer 2-WNbN/WNbC coating, which utilized a higher W arc current (150 A), demonstrated improved phase separation and structural order. On the other hand, the multilayer 3-WNbN/WNbC coating deposited at –120 V showed a smoother surface with well-defined, thinner multilayers, thanks to reduced re-sputtering and enhanced adatom incorporation. Elemental analysis supported these observations, indicating that tungsten content rose with arc current, while nitrogen retention was better at lower bias voltages. Notably, the Nb content consistently surpassed W at lower W arc currents due to greater ionization efficiency and effective plasma transport of Nb atoms.

The structural analysis of monolayer WNbN coatings indicated that the substrate bias voltage significantly influences grain size, phase formation, and the coatings' chemical composition. A low bias voltage of –50 V encouraged the development of nanocrystalline, fine-grained structures, minimizing re-sputtering and enhancing nitrogen incorporation. Consequently, the resulting monolayer WNbN coatings had nearly stoichiometric compositions with slight contributions from hexagonal secondary phases. Increasing the substrate bias to –100 V led to improved crystallinity in the monolayer WNbN coating, as evidenced by sharper, more distinct XRD peaks. The increased surface diffusion from moderate ion bombardment fostered grain growth, revealing a more defined cubic NaCl-type structure, along with recognizable phase separation between W-rich and Nb-rich areas. Although minor hexagonal phase peaks remained, they were less obvious than those observed at lower bias levels. At the extreme bias voltage of –200 V, the intense ion bombardment greatly enhanced film densification, increased re-nucleation frequency, and contributed to surface reorganization. This resulted in the formation of larger grains (15 – 20 nm), a well-textured cubic WNbN phase, and a noticeable reduction in nitrogen content due to re-sputtering effects. The occurrence of hexagonal W_2N/Nb_2N became more apparent under these conditions, indicating nitrogen deficiency at elevated ion energies. Furthermore, despite tungsten's substantial atomic mass, Nb-rich compositions were commonly identified, attributed to superior ionization efficiency of Nb, mobility, and angular plasma exposure.

The structural analysis of the multilayer WNbN/WNbC coatings revealed that all coatings predominantly consisted of cubic phases (WNbN and WNbC/NbC), exhibiting NaCl-type B1 structures. Major reflections at (111), (200), (220), and (311) confirmed the formation of well-crystallized cubic domains. The presence of overlapping or broad peaks was attributed to grain size reduction, stress effects, and minor contributions from the hexagonal phase. In the multilayer 1-WNbN/WNbC coating, the high bias and lower W arc current led to the formation of fine-grained, nanocrystalline structures with significant peak broadening and a noticeable hexagonal phase presence. The multilayer 2-WNbN/WNbC coating benefited from increased W ion flux, yielding improved crystalline quality and stronger cubic phase reflections. The multilayer 3-WNbN/WNbC coating demonstrated the most refined multilayer architecture, marked by enhanced crystallinity, reduced stress, and diminished hexagonal phase content, owing to the optimal combination of high W arc current and moderate bias voltage.

This comprehensive investigation highlights the versatility of cathodic arc evaporation for engineering high-performance WNbN/WNbC nanocomposite coatings. The ability to fine-tune bias voltage and arc current provides a powerful mechanism to control morphology, grain size, phase formation, and elemental distribution. These insights establish a solid foundation for optimizing multilayer coating architectures for advanced applications, including protective, diffusion barrier, or thermal shielding layers in extreme environments.

Acknowledgments

This project has received funding through the EURIZON project, which is funded by the European Union under grant agreement No.871072. Additional funding was received from the EU NextGenerationEU through the Recovery and Resilience Plan for Slovakia under the project No. 09I03-03-V01-00028 and VEGA – Scientific Grant Agency of the Ministry of Education, Research, Development and Youth of the Slovak Republic and the Slovak Academy of Sciences, grant number 1/0345/22.

ORCID

Olga V. Maksakova, https://orcid.org/0000-0002-0646-6704; **Vyacheslav M. Beresnev,** https://orcid.org/0000-0002-4623-3243;
Serhiy V. Lytovchenko, https://orcid.org/0000-0002-3292-5468; **Denis V. Horokh,** https://orcid.org/0000-0002-6222-4574;
Bohdan O. Mazilin, https://orcid.org/0000-0003-1576-0590; **Inna Afanasieva,** https://orcid.org/0000-0002-9523-9780;
Mária Čaplovičová, https://orcid.org/0000-0003-4767-8823; **Martin Sahul,** https://orcid.org/0000-0001-9472-500X.

REFERENCES

[1] Z. Zhang, X. Wang, Q. Zhang, Y. Liang, L. Ren, and X. Li, Opt. Laser Technol. **119**, 105622 (2019). https://doi.org/10.1016/j.optlastec.2019.105622
[2] O. Kessler, T. Herding, F. Hoffmann, and P. Mayr, Surface and Coatings Technology, **182**(2-3), 184 (2004). https://doi.org/10.1016/j.surfcoat.2003.08.054
[3] Y. Zhao, T. Yu, C. Guan, J. Sun, and X. Tan, Ceramics International, **45**(16), 20824 (2019). https://doi.org/10.1016/j.ceramint.2019.07.070
[4] J. Deng, J. Liu, Z. Ding, and M. Niu, Materials & Design, **29**(9), 1828 (2008). https://doi.org/10.1016/j.matdes.2008.03.007
[5] E. Atar, E.S. Kayali, and H. Cimenoglu, Tribology International, **39**(4), 297 (2006). https://doi.org/10.1016/j.triboint.2005.01.038
[6] H.J. Ramos, and N.B. Valmoria, Vacuum, **73**(3-4), 549(2004). https://doi.org/10.1016/j.vacuum.2003.12.158

[7] A. Bendavid, P.J. Martin, T.J. Kinder, and E.W. Preston, Surface and Coatings Technology, **163-164**, 347 (2003). https://doi.org/10.1016/S0257-8972(02)00623-0
[8] T. Zhang, J.H. Song, X.B. Tian, P.K. Chu, and I.G. Brown, J. Vac. Sci. Technol. **A19**, 2048 (2001). https://doi.org/10.1116/1.1372896
[9] K.-W. Kim, B.J. Kim, S.H. Lee, T. Nasir, H.K. Lim, I.J. Choi, B.J. Jeong, *et al*., Coatings, **8**(11), 379 (2018). https://doi.org/10.3390/coatings8110379
[10] B.-R. Kim, K.-D. Woo, J.-K. Yoon, J.-M. Doh, and I.-J. Shon, Journal of Alloys and Compounds, **481**(1-2), 573 (2009). https://doi.org/10.1016/j.jallcom.2009.03.036
[11] D.T. Quinto, in: *50th Annual Technical Conference Proceedings*, 5-11 (2007), pp. 5-11. https://www.svc.org/clientuploads/directory/resource_library/07_005.pdf
[12] J. Ratajski, W. Gulbiński, J. Staśkiewicz, *et al*., Journal of Achievements in Materials and Manufacturing Engineering, **37**(2), 668 (2009). http://jamme.acmsse.h2.pl/papers_vol37_2/37263.pdf
[13] N. Nedfors, O.E. Tengstrand, E. Lewin, *et al*., Surface & Coatings Technology. **206**(2-3), 354 (2011). https://doi.org/10.1016/j.surfcoat.2011.07.021
[14] K. Bobzin, N. Bagcivan, P. Immich, *et al*., Thin Solid Films, **517**(3), 1251 (2008). https://doi.org/10.1016/j.tsf.2008.06.050
[15] C. Zhao, X. Xing, J. Guo, Z. Shi, Y. Zhou, X. Ren, and Q. Yang, Journal of Alloys and Compounds, **788**, 852 (2019). https://doi.org/10.1016/j.jallcom.2019.02.284
[16] T. Dash, and B.B. Nayak, Ceramics International, **45**(4), 4771 (2018). https://doi.org/10.1016/j.ceramint.2018.11.170
[17] B. Osinger, O. Donzel-Gargand, S. Fritze, U. Jansson, and E. Lewin, Vacuum, **224**, 113146 (2024). https://doi.org/10.1016/j.vacuum.2024.113146
[18] Y. Chen, J. Shen, and N. Chen, Solid State Communications, **149**(3-4), 121 (2009). https://doi.org/10.1016/j.ssc.2008.11.004
[19] K.V. Chauhan, and S.K. Rawal, Procedia Technology, **14**, 430 (2014). https://doi.org/10.1016/j.protcy.2014.08.055
[20] M. Ghufran, G.M. Uddin, S.M. Arafat, M. Jawad, and A. Rehman, Proceedings of the Institution of Mechanical Engineers, Part J: Journal of Engineering Tribology, **235**(1), 196 (2020). https://doi.org/10.1177/1350650120933412
[21] R. Haubner, M. Lessiak, R. Pitonak, A. Köpf, and R. Weissenbacher, International Journal of Refractory Metals and Hard Materials, **62B**, 210 (2017). https://doi.org/10.1016/j.ijrmhm.2016.05.009
[22] A.R. Naghashzadeh, A. Shafyei, and F. Sourani, J. of Mater. Eng. and Perform. **31**, 4335 (2022). https://doi.org/10.1007/s11665-021-06533-2
[23] A. Pogrebnjak, K. Smyrnova, and O. Bondar, Coatings, **9**(3), 155, (2019). https://doi.org/10.3390/coatings9030155
[24] J.S. Koehler, Physical Review B, **2**, 547 (1970). https://doi.org/10.1103/PhysRevB.2.547
[25] X. Junhua, G. Mingyuan, and L. Geyang, Journal of Materials Science, **35**, 3535 (2000). https://doi.org/10.1023/A:1004853211220
[26] P.M. Anderson, T. Foecke, and P.M. Hazzledine, MRS Bulletin, **24**, 27 (1999). https://doi.org/10.1557/S0883769400051514
[27] J.C. Caicedo, A. Guerrero, and W. Aperador, Vacuum, **143**, 217 (2017). https://doi.org/10.1016/j.vacuum.2017.06.015
[28] Y. Li, Q. Ye, Y. Zhu, *et al*., Surface and Coatings Technology, **362**, 27 (2019). https://doi.org/10.1016/j.surfcoat.2019.01.091
[29] A.D. Pogrebnjak, V.I. Ivashchenko, P.L. Skrynskyy, *et al*., Composites Part B: Engineering, **142**, 85 (2018). https://doi.org/10.1016/j.compositesb.2018.01.004
[30] A. González-Hernández, A.B. Morales-Cepeda, M. Flores, *et al*., Coatings, **11**(7), 797 (2021). https://doi.org/10.3390/coatings11070797
[31] S. Zhang, E. Byon, M. Li, *et al*., Thin Solid Films, **519**(6), 1901 (2011). https://doi.org/10.1016/j.tsf.2010.10.024
[32] I. V. Serdyuk, V. O. Stolbovyi, A. V. Dolomanov, and V. M. Domnych, Metallofiz. Noveishie Tekhnol. **44**(4), 547 (2022). (in Ukrainian). https://doi.org/10.15407/mfint.44.04.0547
[33] O.V. Maksakova, V.M. Beresnev, S.V. Lytovchenko *et al*., East European Journal of Physics, (1), 396 (2025). https://doi.org/10.26565/2312-4334-2025-1-49

ВПЛИВ УМОВ ОСАДЖЕННЯ НА МІКРОСТРУКТУРУ ТА СКЛАД МОНОШАРОВИХ НІТРИДНИХ ТА КАРБІДНО-НІТРИДНИХ МУЛЬТИШАРОВИХ ПОКРИТТІВ НА ОСНОВІ W ТА Nb

О.В. Максакова[a,b], В.М. Береснєв[b], С.В. Литовченко[b], Д.В. Горох[b], Б.О. Мазілін[b], І.О. Афанасьєва[b,d], М. Чапловичова[c], М. Сахул[a]

[a]*Інститут матеріалознавства, Словацький технологічний університет у Братиславі, вул Яна Ботту 25, 917 24, Трнава, Словаччина*
[b]*В.Н. Харківський національний університет імені Каразіна, пл. Свободи, 4, 61000 Харків, Україна*
[c]*Центр нанодіагностики матеріалів, Словацький технологічний університет у Братиславі, Вазовова 5, 812 43, Братислава, Словаччина*

У роботі досліджено структурну та композиційну еволюцію моношарових покриттів WNbN та багатошарових покриттів WNbN/WNbC, осаджених методом катодного дугового випаровування. Вплив напруги зміщення підкладки (від -50 В до -200 В) і струму катодної дуги (130 - 150 А для W, 110 - 120 А для Nb) систематично вивчався з метою адаптації морфології покриттів, фазоутворення та розподілу елементів. Мікроструктурний аналіз поперечного перерізу виявив псевдобагатошарові структури всередині моношарів через обертання підкладки та обмежену взаємодифузію. Збільшення напруги зміщення сприяло ущільненню, подрібненню зерен і покращенню адгезії, але також посилювало повторне розпилення азоту, впливаючи на стехіометрію і швидкість осадження. Багатошарові покриття демонстрували чітке чергування шарів нітридів і карбідів, причому на морфологію і кристалічність сильно впливала енергія іонів і утворений потік іонів металу. Структурний аналіз підтвердив домінування кубічних твердих розчинів на основі WNbN і WNbC з незначною кількістю гексагональних W_2N і Nb_2N. Розмір зерен коливався від 6 до 15 нм в залежності від параметрів осадження. Оптимальна структура була досягнута при помірному зміщенні (-120 В) і високому струмі дуги W, що дозволило отримати однорідні шари, збалансований склад і підвищену кристалічність. Результати демонструють, як контрольовані параметри процесу дозволяють створювати високоефективні нанокомпозитні покриття з регульованою мікроструктурою і фазовим складом, придатні для захисних застосувань.

Ключові слова: *багатошарові покриття; нітриди; карбіди; ніобій; вольфрам; мікроструктура; склад*